International Journal of Civil Engineering

Hydraulic Structure

Evaluation of turbulence models in the simulation of oblique standing shock waves in supercritical channel flows

E. Alamatian[1], M. R. Jaefarzadeh[2,*]

Received: April 2010, Revised: December 2011, Accepted: February 2012

Abstract

In this article, the two-dimensional depth-averaged Saint Venant equations, including the turbulence terms, are solved in a supercritical flow with oblique standing waves. The algorithm applies the finite volume Roe-TVD method with unstructured triangular cells. Three depth-averaged turbulence models, including the mixing length, k-ε and algebraic stress model (ASM), are used to close the hydrodynamic equations. The supercritical flow in a channel downstream from a side-baffle in plan is then simulated, and the numerical results are compared with the data obtained from a laboratory model. The application of different models demonstrates that the consideration of turbulence models improves the results at the shock wave positions. The qualitative study of the results and error analysis indicates that the ASM offers the most desirable solutions in comparison with the other models. However, our numerical experiments show that, amongst the source term components, the negligence of turbulence terms produces the least error in the depth estimation in comparison with the removal of the bed slope or bed friction terms.

Keywords: Finite volume method, Mixing length model, k-ε model, Algebraic stress model, Oblique standing waves

1. Introduction

In general, a broad class of flow types, including river flows, tsunami waves and dambreak flows, are defined as shallow flows where the scale of the water depth is much less than the characteristic length scales in the horizontal direction. In other words, the shallow water depth prevents the development of three-dimensional turbulent structures and confines the secondary flows caused by the expansion of small eddies. Therefore, the turbulent shallow flows may be studied quasi two-dimensionally. By neglecting the development of turbulence in the vertical direction, the Navier-Stokes equations may be integrated and averaged in depth to reduce the number of unknowns and to simplify the equations considerably.

Several methods have been developed for taking the turbulence effects into consideration, ranging from simple mixing length theory to Reynolds average Navier Stokes (RANS) equations, large eddy simulations (LES) and direct numerical simulations (DNS). The latter two models require high computational effort and are not suitable for engineering problems. The RANS approach, however, has been extensively adopted for turbulence modeling. In the majority of the RANS models, Reynolds stresses are calculated based on the Boussinesq theory, which assumes a linear relationship between the stresses and the gradients of the main flow variables, [1].

Kraichnan [2] and Batchelor [3] were amongst the early researchers in the late 60's who studied the two-dimensional turbulent flows. Kraichnan studied the behavior of the energy spectrum in the inertial subrange in quasi-steady forced 2D turbulence, while Batchelor studied the energy spectrum in homogeneous decaying 2D turbulence. The studies conducted by Dracos et al. [4], Giger et al. [5], Chen and Jirka [6], Thomas and Goldschmidt [7] and Lloyd et al. [8], indicated that large horizontal quasi-2D coherent structures play an important role in the development of shallow flow characteristics.

The homogeneous decaying turbulence produced by a grid in shallow flows was investigated by Uijttewaal and Jirka, [9]. They explained the mode of energy transfer and the merging of vortices. Several studies have been conducted by Uijttewaal and Booij [10], Uijttewaal and Tukker [11] and Chu and Babarutsi [12] concerning the shallowness and bed friction effects in the development of 2D turbulent structures in free

* *Corresponding Author: jafarzad@um.ac.ir*
1 Assistant Professor, Department of Civil Engineering, Khavaran Institute of Higher Education, Mashhad, Iran
2 Corresponding author: Professor, Department of Civil Engineering, School of Engineering, Ferdowsi University of Mashhad, Mashhad, Iran

surface mixing layers. All of these numerical and experimental studies have confirmed that large 2D turbulent structures are equally important as slope and bed friction effects. The stability of large turbulent structures depends mainly on a balance between the horizontal shear stresses and the effects caused by the bed friction and vertical stresses. Therefore, in shallow flows, some of the characteristics are not two-dimensional.

Comparatively, amongst the studies that have been conducted using the RANS models, insufficient attention has been paid to the two-dimensional, depth-averaged shallow water equations (2D-SWE), [13]. In these equations, the turbulence effects and bed frictions may be included in the source terms equally. The first zero-equation model that explained the turbulence viscosity distribution was proposed by Prandtl [1] and was called the Prandtl mixing length model. The depth-averaged version of this model has been widely used in the literature, [15]. Rastogi and Rodi [16] applied a two-equation depth-averaged k-ε model for the turbulence energy and the rate of energy dissipation. This model is the most popular depth-averaged turbulence model for the shallow water equations. However, the main drawback of the eddy viscosity models may be attributed to the Boussinesq assumption of isotropic eddy viscosity. This prerequisite has been removed in the turbulence stress models. Cea et al. [17] presented a depth-averaged algebraic stress model in which the effect of the bed friction was included as well. Their model offered reasonable stability in numerical experiments.

Applying the finite volume method (FVM), the integral forms of the conservation laws are discretized over the computational domain into small structured/unstructured cells. Here, the main objective is to find the normal fluxes at the faces of the cells, [18].

An initial value problem for conservation laws, with the initial data given by a piecewise constant function with a single jump discontinuity, is called a Riemann problem. Utilizing the weak solution theory of hyperbolic conservation laws, exact Riemann solvers are able to trace the propagation of discontinuities conveniently, including the shock waves in a solution domain, [18,19]. However, the implementation of these algorithms in the Godunov scheme is inefficient for non-linear systems. On the other hand, approximate Riemann solvers initiated, for example by Roe [20], Osher and Solomon [21], Harten et al. [22] and Einfeldt [23], amongst the others, offer more efficient results. Specifically, the flux difference splitting algorithm of Roe has been widely applied and recommended for the shallow water equations, [17,18,24].

The main consequence of the turbulence terms is the diffusion of the velocity field, which is a physical phenomenon that may erroneously be appraised when it is intensified by a numerical diffusion. The unrealistic numerical diffusion is inherent to the upwind schemes that are commonly used for solving the hyperbolic equations. Therefore, the implementation of high resolution schemes for the convective fluxes to minimize the numerical diffusion has been highly recommended, [13]. To achieve a high resolution in the advanced FVM of the Godunov type and to eliminate false oscillations or wiggles at the discontinuities, the flux or slope limiters may be used for the data reconstruction at the face of each cell. This method is called the total variation diminishing (TVD) method, [19].

Cea [25] applied a second order finite volume Roe-TVD scheme to the shallow water equations with wet-dry fronts, including the turbulence terms. In the present article, we apply a similar model to simulate the oblique standing shock waves produced by the incidence of a supercritical flow to a side-baffle in an open channel. The multidimensional slope-limiters of Yoon and Kang [26] are employed to achieve the second-order spatial accuracy and to prevent spurious oscillations. For the inspection of the turbulence effects, several depth-averaged version of the RANS models, such as the two-dimensional mixing length model, k-ε model and algebraic stress model (ASM), are examined. The numerical results are compared with the data obtained from a laboratory flume to verify the accuracy of the computations.

2. Shallow water equations

The two-dimensional, depth-averaged shallow water equations may be obtained by integrating the 3D Navier–Stokes equations over the flow depth with the assumptions of incompressible fluid, a hydrostatic pressure distribution, a nearly uniform velocity distribution in the vertical direction and a small bottom slope. The conservative form of the depth-averaged shallow water equations with source terms may be written in vectorial form as:

$$\frac{\partial W}{\partial t}+\frac{\partial F_x}{\partial x}+\frac{\partial F_y}{\partial y}=\sum_{k=1}^{3}G_k \tag{1}$$

in which

$$W=\begin{pmatrix} h \\ q_x \\ q_y \end{pmatrix} \;;\; F_x=\begin{pmatrix} q_x \\ \frac{q_x^2}{h}+\frac{gh^2}{2} \\ \frac{q_x q_y}{h} \end{pmatrix} \;;\; F_y=\begin{pmatrix} q_y \\ \frac{q_x q_y}{h} \\ \frac{q_y^2}{h}+\frac{gh^2}{2} \end{pmatrix} \tag{2}$$

where W is the vector of the conserved variables, including the water depth h and the unit discharges q_x and q_y . The vectors F_x and F_y account for the convective fluxes in the x- and y- directions, respectively, and g is the acceleration due to gravity. The vector G_k is a source term composed of the bed slope G_1, bed friction G_2, and turbulence terms G_3:

$$G_1=\begin{pmatrix} 0 \\ -gh\frac{\partial Z_b}{\partial x} \\ -gh\frac{\partial Z_b}{\partial y} \end{pmatrix} \;;\; G_2=\begin{pmatrix} 0 \\ -\frac{\tau_{b,x}}{\rho} \\ -\frac{\tau_{b,y}}{\rho} \end{pmatrix} \;;\; G_3=\begin{pmatrix} 0 \\ -\frac{\partial h\overline{u_i'u_j'}}{\partial x} \\ -\frac{\partial h\overline{u_i'u_j'}}{\partial y} \end{pmatrix} \quad (i,j=1,2) \tag{3}$$

where Z_b is the bed elevation, $\tau_{b,x}$ and $\tau_{b,y}$ are the bed shear stresses due to friction in the x- and y- directions, ρ is the fluid density, and $\overline{u_i'u_j'}$ are the depth-averaged horizontal Reynolds stresses.

3. Numerical solution

By time discretization of the system (1) and simplification, the following equations are obtained with a second-order of

accuracy in time, [25]:

$$W^{n+\frac{1}{2}} = W^n - \frac{\Delta t}{2}\left(\frac{\partial F_x}{\partial x}(W^n) + \frac{\partial F_y}{\partial y}(W^n)\right) + \frac{\Delta t}{2}\sum_{k=1}^{3} G_k^n$$
$$W^{n+1} = W^n - \Delta t\left(\frac{\partial F_x}{\partial x}\left(W^{n+\frac{1}{2}}\right) + \frac{\partial F_y}{\partial y}\left(W^{n+\frac{1}{2}}\right)\right) + \Delta t\sum_{k=1}^{3} G_k^{n+\frac{1}{2}} \quad (4)$$

where W^n is the vector of conserved variables at time t^n, and Δt is the time step. For spatial discretization, an upwind model may be implemented. The integration of system (1) over a cell i with area A_i and implementation of the Gauss divergence theorem lead to:

$$A_i \frac{W_i^{n+1} - W_i^n}{\Delta t} + \int_{L_i}\left(F_x\,\tilde{n}_x + F_y\,\tilde{n}_y\right)dL = \sum_{k=1}^{3}\int_{C_i} G_k\,dA \quad (5)$$

where L_i is the boundary of the cell i, and $\tilde{n}=(\tilde{n}_x, \tilde{n}_y)$ is the unit vector normal to the cell face, Fig. 1-a. The second term on the left hand side of Eq. (5) may be written as:

$$\int_{L_i}\left(F_x\,\tilde{n}_x + F_y\,\tilde{n}_y\right)dL = \sum_{j\in K_i}\int_{L_{ij}}\left(F_x\,\tilde{n}_x + F_y\,\tilde{n}_y\right)dL = \sum_{j\in K_i}\phi_{ij}(W_i, W_j, n_{ij}) \quad (6)$$

where K_i is the number of faces at cell i (in a triangular cell, K_i=3), L_{ij} is the length of the face between cells i and j (cell face ij), ϕ_{ij} is the numerical flux at the cell face ij, and $n_{ij}=(n_x,n_y)_{ij}$ is the normal vector at the cell face ij with a length of L_{ij}. In the upwind method, the numerical flux is defined as:

$$\phi_{ij} = \frac{Z(W_i, n_{ij}) + Z(W_j, n_{ij})}{2} - \frac{1}{2}\left|\phi\left(W_i, W_j, n_{ij}\right)\right|\left(W_j - W_i\right)$$
$$|\phi| = X|D|X^{-1} \quad ; \quad Z = F_x n_x + F_y n_y \quad (7)$$
$$|D| = \begin{bmatrix} |\overline{\lambda}_1| & 0 & 0 \\ 0 & |\overline{\lambda}_2| & 0 \\ 0 & 0 & |\overline{\lambda}_3| \end{bmatrix} \quad ; \quad X = \begin{bmatrix} 0 & 1 & 1 \\ -\tilde{n}_y & \overline{U}_x + \overline{C}\,\tilde{n}_x & \overline{U}_x - \overline{C}\,\tilde{n}_x \\ \tilde{n}_x & \overline{U}_y + \overline{C}\,\tilde{n}_y & \overline{U}_y - \overline{C}\,\tilde{n}_y \end{bmatrix}$$
$$\overline{\lambda}_1 = n_x\overline{U}_x + n_y\overline{U}_y \quad ; \quad \overline{\lambda}_2 = \overline{\lambda}_1 + \overline{C}\,L_{ij} \quad ; \quad \overline{\lambda}_3 = \overline{\lambda}_1 - \overline{C}L_{ij}$$

The averaged values in the first order scheme of Roe at each cell are defined as:

$$\overline{U}_x = \frac{\sqrt{h_i}U_{x,i} + \sqrt{h_j}U_{x,j}}{\sqrt{h_i} + \sqrt{h_j}} \; ; \overline{U}_y = \frac{\sqrt{h_i}U_{y,i} + \sqrt{h_j}U_{y,j}}{\sqrt{h_i} + \sqrt{h_j}} \; ; \; \overline{C} = \sqrt{g\frac{h_i + h_j}{2}} \quad (8)$$

where $U_{x,i}$ and $U_{y,i}$ are the velocities of the flow in cell i in the x- and y- directions, respectively, and h_i is the water depth in cell i. To achieve a second order accuracy in the method of Roe, the conserved variables at the triangular cell faces are reconstructed using a spatial limiting technique [26], Fig. 1-b:

$$W_{Ij} = W_i + r\nabla_i^1 W \quad (9)$$

in which W_{Ij} is the value of W_i at the boundary with cell j, r is the distance vector between the cell area center i and the middle of L_{ij} , and ∇_i^1 is the limited gradient of variables at cell i, defined by:

$$\nabla_i^1 W = w_a\nabla W_a + w_b\nabla W_b + w_c\nabla W_c \quad (10)$$

where w_a, w_b and w_c are weighting factors, and ∇w_a, ∇w_b and ∇w_c are unlimited gradients of the three surrounding cells a, b and c. The unlimited gradient for cell i is computed using the area-weighted average gradients at the three faces:

$$\nabla W_i = \frac{A_{i1a2}(\nabla W)_1 + A_{i2b3}(\nabla W)_2 + A_{i3c1}(\nabla W)_3}{A_{i1a2} + A_{i2b3} + A_{i3c1}} \quad (11)$$

where A_{i1a2} is the area of quadrilateral $i1a2$ (Fig. 1-a), and $\nabla(W)_m$ is the gradient of the variable W at the face m of cell i. This gradient may be computed from the divergence theorem and area-weighted average of two triangles around each face. For example, for face 1 in Fig. 1-a, we have:

$$(\nabla W)_1 = \frac{A_{1a2}\nabla W|_{1a2} + A_{1i2}\nabla W|_{1i2}}{A_{1a2} + A_{1i2}} \; ; \quad \nabla W|_{1a2} = \frac{1}{A_{1a2}}\oint_\Gamma W n d\Gamma \quad (12)$$

in which Γ is the integral path along the circumference of each sub-triangle (e.g., 1a2). The weighting functions w_a, w_b and w_c are defined as:

$$w_a = \frac{\left(g_b g_c + \varepsilon^2\right)}{\left(g_a^2 + g_b^2 + g_c^2 + 3\varepsilon^2\right)} \quad ; \quad w_b = \frac{\left(g_a g_c + \varepsilon^2\right)}{\left(g_a^2 + g_b^2 + g_c^2 + 3\varepsilon^2\right)}$$
$$w_c = \frac{\left(g_a g_b + \varepsilon^2\right)}{\left(g_a^2 + g_b^2 + g_c^2 + 3\varepsilon^2\right)} \quad (13)$$

where ε is a small value (on the order of 10^{-4} and less), and g_a, g_b and g_c are the functions of the gradients of variables in the cells surrounding cell i (i.e., cells a, b and c in Fig. 1-a) defined by:

$$g_a = \|\nabla W_a\|_2^2 \quad ; \quad g_b = \|\nabla W_b\|_2^2 \quad ; \quad g_c = \|\nabla W_c\|_2^2 \quad (14)$$

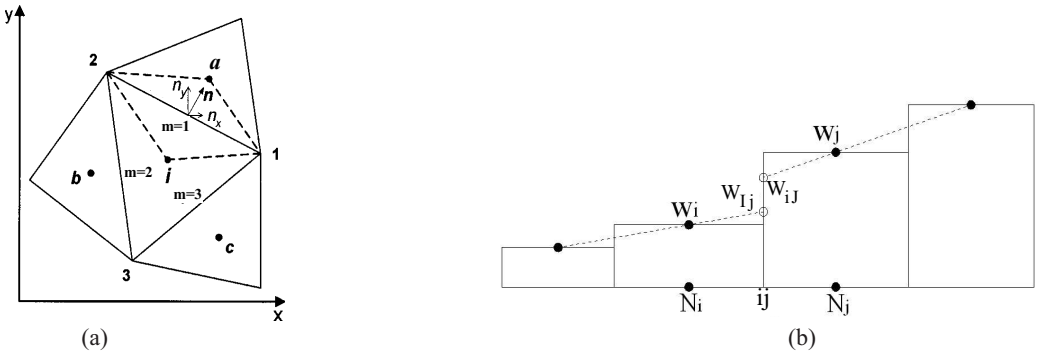

(a) (b)

Fig. 1. (a) A typical control volume cell. (b) Reconstruction of the conservative variables from the cell centers to the cell faces

In Eqs. (14), $||\nabla W||_2^2$ is the second norm of the unlimited gradient of a specified variable. By definition, the norm L_2 of a vector is the sum of the squares of its elements. Using the above equations, the limited gradient of a variable may be determined, and the data may be reconstructed at the cell boundaries.

The slope and friction source terms, G_1 and G_2, in Eqs. (3) may be defined as, [25]:

$$G_1 = \begin{pmatrix} 0 \\ -ghS_{0x} \\ -ghS_{0y} \end{pmatrix} \;;\; G_2 = \begin{pmatrix} 0 \\ -c_f U_x |U_x| \\ -c_f U_y |U_y| \end{pmatrix} \;;\; c_f = \frac{gn^2}{h^{1/3}} \tag{15}$$

where S_{0x} and S_{0y} are the bed slopes in the x- and y- directions, respectively, c_f is the bed coefficient of friction, and n is the Manning roughness. During the numerical computations, G_1 and G_2 are calculated based on the data obtained for the cell centers.

4. Depth-averaged Reynolds stress models for 2D free surface flow

The Boussinesq assumption is the basis of all of the turbulence eddy viscosity models. It relates the Reynolds stresses to the mean velocity gradients via the eddy viscosity. Using this assumption in the averaged Reynolds stress models, the effects of the Reynolds stresses in the shallow flows (G_3 in Eq. (3)) may be written as:

$$G_3 = \begin{pmatrix} 0 \\ \frac{\partial}{\partial x}\left(\upsilon_t h \frac{\partial U_x}{\partial x}\right) + \frac{\partial}{\partial y}\left(\upsilon_t h \frac{\partial U_x}{\partial y}\right) \\ \frac{\partial}{\partial x}\left(\upsilon_t h \frac{\partial U_y}{\partial x}\right) + \frac{\partial}{\partial y}\left(\upsilon_t h \frac{\partial U_y}{\partial y}\right) \end{pmatrix} \tag{16}$$

where υ_t is the turbulence eddy viscosity. To discretize this term, a semi-implicit method may be applied. When the viscosity is large, it is required to discretize the diffusive term implicitly. Davidson [27] divided this term in two parts:

$$G_3 = G_{3,\perp} + G_{3,\parallel} \tag{17}$$

where $G_{3,\perp}$ is the orthogonal viscosity, and $G_{3,\parallel}$ is the non-orthogonal viscosity. For the momentum component in the x-direction, the two components of viscosity may be calculated from, [27]:

$$G_{3,\perp,x} = \sum_{j \in K_i} \Gamma_{D_\perp} U_{x,j} - \frac{\Gamma_{D_\perp}}{h_i} q_{x,i} \tag{18-a}$$

$$G_{3,||,x} = \sum_{j \in K_i} \upsilon_{t,ij} h_{ij} \frac{d_{ij}}{d_{\perp,ij}} \left(U_{x,B} - U_{x,V}\right)\left(\tilde{\alpha}_{x,ij}\tilde{n}_{x,ij} + \tilde{\alpha}_{y,ij}\tilde{n}_{y,ij}\right) \tag{18-b}$$

in which $\Gamma_{D_\perp} = \upsilon_{t,ij} h_{ij} \frac{|n_{ij}|}{d_{\perp,ij}}$ is the orthogonal diffusion, $q_{x,i}$ is the unit discharge at a cell i in the x-direction, h_{ij} and $\upsilon_{t,ij}$ are the averages of the depth and turbulent eddy viscosity in cells i and j, $U_{x,B}$ and $U_{x,V}$ are velocities in the x-direction at points B and V in Fig. 2, $\tilde{\alpha}_{ij}=(\tilde{\alpha}_{x,ij}, \tilde{\alpha}_{y,ij})$ is a unit vector perpendicular to the line that connects the centers of the cells i and j, and $d_{\perp,ij}$ is the projection of the distance between the two cell centers i and j over a line perpendicular to the common face of the two cells. All of the variables in Eqs. (18) are evaluated at time t^n except the unit discharge $q_{x,i}$, which is calculated at t^{n+1}. Therefore, no additional system of equations must be solved to increase the computational cost. The turbulence terms in the y-direction may be calculated similarly.

In the above equations, the eddy viscosity term may be computed using any of the turbulence modeling theories that will be introduced in the following sections.

4.1. The depth-averaged mixing length model

In this model, the turbulence eddy viscosity is given by, [15]:

$$\upsilon_t = l_s^2 \sqrt{2\left(\frac{\partial U_x}{\partial x}\right)^2 + 2\left(\frac{\partial U_y}{\partial y}\right)^2 + \left(\frac{\partial U_x}{\partial y} + \frac{\partial U_y}{\partial x}\right)^2 + \left(2.34\frac{u_f}{\kappa h}\right)^2} \tag{19}$$

$$l_s = \min(0.267\kappa h, \kappa d_{wall})$$

in which l_s is the mixing length, U_x (U_y) is the flow velocity in the x (y) direction, κ=.41 is the von Karman constant, d_{wall} is the distance of the cell center to the nearest wall, and u_f is the shear velocity that may be obtained from:

$$u_f = \sqrt{c_f\left(U_x^2 + U_y^2\right)} \tag{20}$$

4.2. The depth-averaged k-ε model

In the depth-averaged model of k-ε, two transport equations may be solved to calculate the turbulence eddy viscosity. One of these equations computes the turbulence kinetic energy (k), and the other determines the dissipation rate of turbulent kinetic energy (ε). The k-ε system of equations in conservative vectorial form may be written as, [17]:

$$\frac{\partial \Phi}{\partial t} + \frac{\partial F_{\Phi,x}}{\partial x} + \frac{\partial F_{\Phi,y}}{\partial y} = \sum_{m=1}^{4} H_m \tag{21}$$

where Φ is the vector of the turbulence conservative variables, and $F_{\Phi,x}$ and $F_{\Phi,y}$ are the physical fluxes in the x- and y-directions, defined as:

$$\Phi = \begin{pmatrix} hk \\ h\varepsilon \end{pmatrix} \;;\; F_{\Phi,x} = \begin{pmatrix} hkU_x \\ h\varepsilon U_x \end{pmatrix} = U_x \Phi \;;\; F_{\Phi,y} = \begin{pmatrix} hkU_y \\ h\varepsilon U_y \end{pmatrix} = U_y \Phi \tag{22}$$

The source term elements, H_m(m=1,4) , are composed of the turbulent diffusion (H_1), the production due to the horizontal

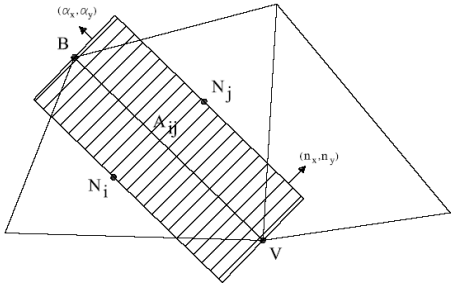

Fig. 2. Discretisation of the turbulent diffusion term

velocity gradient (H_2), the production due to bed friction (H_3), and the dissipation rate (H_4). These terms are defined as:

$$H_1=\begin{pmatrix}\frac{\partial}{\partial x_j}\left(\frac{\upsilon_t}{\sigma_k}h\frac{\partial k}{\partial x_j}\right)\\ \frac{\partial}{\partial x_j}\left(\frac{\upsilon_t}{\sigma_\varepsilon}h\frac{\partial \varepsilon}{\partial x_j}\right)\end{pmatrix};\ H_2=\begin{pmatrix}\min\left(2\upsilon_t S_{ij}S_{ij}h,10\varepsilon h\right)\\ c_{1\varepsilon}\frac{\varepsilon}{k}2\upsilon_t S_{ij}S_{ij}h\end{pmatrix};\ H_3=\begin{pmatrix}\min\left(c_k u_f^3,10\varepsilon h\right)\\ c_\varepsilon\frac{u_f^4}{h}\end{pmatrix}$$

$$H_4=\begin{pmatrix}-\varepsilon h\\ -c_{2\varepsilon}\frac{\varepsilon^2}{k}h\end{pmatrix};\ S_{ij}=\frac{1}{2}\left(\frac{\partial U_i}{\partial x_j}+\frac{\partial U_j}{\partial x_i}\right);\ i,j=1,2\ ;\ \upsilon_t=c_\mu\frac{k^2}{\varepsilon} \quad (23)$$

Where S_{ij} is the horizontal mean strain-rate tensor and is calculated using the depth-averaged velocities. The coefficients $c_{1\varepsilon}$, $c_{2\varepsilon}$, σ_k, c_μ and σ_ε are constants of the model, and their values for the standard k-ε are given as, [28]:

$$c_{1\varepsilon}=1.44\ ;\ c_{2\varepsilon}=1.92\ ;\ \sigma_k=1.0\ ;\ c_\mu=0.09\ ;\ \sigma_\varepsilon=1.31 \quad (24)$$

The k-ε system of partial differential equations in its conservative form is of hyperbolic type with source terms. Both of the eigenvalues of the Jacobian matrix of fluxes are equal, which simplifies the numerical scheme. For the solution of this system, the turbulent diffusion term (H_1) may be split into two parts: an orthogonal diffusion term ($H_{1,\perp}$) and a non-orthogonal diffusion term ($H_{1,\parallel}$). Based on Davidson's proposal [27] for preserving the stability of the method and maintaining positive turbulence variables during the numerical computation, the source term may be divided into a positive and a negative part. After some algebraic manipulation we obtain:

$$\Phi_i^{n+1}\left(1-H_{N,i}^n\right)=\left(1-\frac{\Delta t}{A_i}a_i^n\right)\Phi_i^n+\frac{\Delta t}{A_i}\sum_{j\in K_i}a_{ij}^n\Phi_j^n+\Delta t H_{p,i}^n \quad (25)$$

where $H^n_{p,i}$ and H^n_{Ni} are the positive and negative parts of the source terms, respectively. The values of a^n_{ij} and a^n_i are computed as:

$$a_i^n=\sum_{j\in K_i}\left(\frac{\lambda_{ij}+|\lambda_{ij}|}{2}+\Gamma_{D_{\perp,ij}}\right)\quad ;\quad a_{ij}^n=\frac{-\lambda_{ij}+|\lambda_{ij}|}{2}+\Gamma_{D_{\perp,ij}} \quad (26)$$

Normally, the source terms H_2 and H_3 are always positive, and the loss term H_4 is negative. However, the diffusive source term $H_{1,\parallel}$ may be either positive or negative. Therefore, it may be added to the H^n_p or H^n_N terms. The negative and positive source terms may be written as:

$$H_N^n=\min\left(\frac{H_{1,\parallel}}{\Phi},0\right)^n+\begin{pmatrix}-\frac{\varepsilon}{k}\\ -c_{2\varepsilon}\frac{\varepsilon}{k}\end{pmatrix}^n \quad (27)$$

$$H_P^n=\max\left(H_{1,\parallel},0\right)^n+H_2^n+H_3^n$$

Where the jet of the flow impinges the sidewalls, the turbulence kinetic energy given by the k-ε model is overestimated. Therefore, a realizability constraint is required to adjust the turbulence eddy viscosity, [29]:

$$\upsilon_t=\min\left(c_\mu\frac{k^2}{\varepsilon},\frac{k}{3}\left(\frac{2}{S_{ij}S_{ij}}\right)^{1/2}\right) \quad (28)$$

4.3. The depth-averaged algebraic stress model (ASM)

In this model, algebraic equations are used to obtain the Reynolds stresses. Although the system of equations in the ASM appears to be simpler than the RANS models, the technique is less stable, specifically in 3D-modeling, because of the highly nonlinear nature of the algebraic equations. The stability of the model improves when explicit methods are used instead of implicit techniques, [30].

In this procedure, only three components of the Reynolds stresses ($\overline{u'^2}$, $\overline{v'^2}$ and $\overline{u'v'}$) appear in the depth-averaged shallow water equations, [17]:

$$\begin{pmatrix}\overline{u'^2}\\ \overline{v'^2}\\ \overline{u'v'}\end{pmatrix}=\frac{1-c_2}{c_{11}}\frac{k}{\varepsilon}\begin{pmatrix}a_{11}&a_{12}&a_{13}\\ a_{21}&a_{22}&a_{23}\\ a_{31}&a_{32}&a_{33}\end{pmatrix}\begin{pmatrix}\overline{u'^2}\\ \overline{v'^2}\\ \overline{u'v'}\end{pmatrix}+\begin{pmatrix}b_1\\ b_2\\ b_3\end{pmatrix} \quad (29)$$

in which c_2=0.6 and c_{11}=1.8 are constant coefficients. The matrix and vector elements, a_{ij} and b_i, are defined as:

$$a_{11}=-\frac{4}{3}\frac{\partial U_x}{\partial x}\quad ;\quad a_{12}=-\frac{2}{3}\frac{\partial U_y}{\partial y}\quad ;\quad a_{13}=-\frac{4}{3}\frac{\partial U_x}{\partial y}+\frac{2}{3}\frac{\partial U_y}{\partial x} \quad (30)$$

$$a_{21}=\frac{2}{3}\frac{\partial U_x}{\partial x}\quad ;\quad a_{22}=-\frac{4}{3}\frac{\partial U_y}{\partial y}\quad ;\quad a_{23}=-\frac{4}{3}\frac{\partial U_y}{\partial x}+\frac{2}{3}\frac{\partial U_x}{\partial y}$$

$$a_{31}=-\frac{\partial U_y}{\partial x}\quad ;\quad a_{32}=-\frac{\partial U_x}{\partial y}\quad ;\quad a_{33}=-\left(\frac{\partial U_x}{\partial x}+\frac{\partial U_y}{\partial y}\right)$$

$$b_1=\frac{2}{3}k+\frac{k}{\varepsilon}\frac{(1-c_2)}{c_{11}}\left(\frac{2}{3}P_{uu,V}-\frac{1}{3}P_{vv,V}\right);$$

$$b_2=\frac{2}{3}k+\frac{k}{\varepsilon}\frac{(1-c_2)}{c_{11}}\left(\frac{2}{3}P_{vv,V}-\frac{1}{3}P_{uu,V}\right);\ b_3=\frac{k}{\varepsilon}\frac{(1-c_2)}{c_{11}}P_{uv,V}$$

where $P_{uu,V}$, $P_{vv,V}$ and $P_{uv,V}$ are the production terms caused by the bed friction and are defined as:

$$P_{uu,V}=2\frac{u_f^2\,q_x^2}{h^3|U|}\ ;\ P_{vv,V}=2\frac{u_f^2\,q_y^2}{h^3|U|}\ ;\ P_{uv,V}=-2\frac{u_f^2\,q_x\,q_y}{h^3|U|} \quad (31)$$

The eddy viscosity assumption may be used to calculate the kinetic turbulence energy to avoid too much dependence of Reynolds stresses on each other and to increase the stability of the method. Therefore, the following equation is implemented in the turbulence production term in the k-ε model (H_2 in Eq. (23)):

$$P_k=2\upsilon_t\left[\left(\frac{\partial U}{\partial x}\right)^2+\frac{1}{2}\left(\frac{\partial U}{\partial y}+\frac{\partial V}{\partial x}\right)^2+\left(\frac{\partial V}{\partial y}\right)^2\right]+\frac{P_{uu,V}+p_{vv,V}}{2} \quad (32)$$

Consequently, the system (29) may be solved explicitly, improving the stability and convergence of the model.

5. Experimental model

Some experiments were carried out in a flume of hydraulic laboratory to examine the behavior of the oblique shock waves downstream of a side-baffle. The flume had a length of L =8.0 m, a width of B =0.4 m and a wall height of H=0.5 m. The longitudinal slope of the flume was S_{0x}=0.00624, with a

measured Manning roughness coefficient of n =0.0104. A thin plate, as a side-baffle, was installed normal to the sidewall of the flume, 3.0 m downstream from the beginning of the flume. The plate width varied from 0.12 to 0.3 m in different experiments. The constant flow discharge was Q=0.0372 m^3/s. The normal depth of flow was measured as 0.07 m without the presence of the baffle. When the side-baffle was fixed, the water rose at the upstream side, and a jet of flow was released to the downstream canal from the partial opening. The impingement of the jet flow to the side walls produced a series of oblique shock waves, as shown in Fig. 3. Moreover, a vortex was generated downstream, next to the baffle. The depth of flow was measured by a depth gauge at distances of 0.04 m in the longitudinal and transversal directions. The measurements were carried out at three longitudinal sections, p_1, p_2 and p_3, at 0.1, 0.2 and 0.3 m from the sidewall and at eight transversal cross sections, as shown in Fig. 4.

6. Application of the numerical model

For the evaluation of the turbulence models, the supercritical flow in a canal, having the same dimensions as the experimental flume, with a side-baffle was simulated. The length of the canal in the numerical model was 5 m, and the solution domain was divided into 8305 unstructured triangular cells. A constant discharge was introduced at the upstream boundary. At the downstream end, the dependant variables (h, q_x and q_y) were interpolated from the solution domain, which is reasonable due to the supercritical nature of the flow. The solid boundaries were simulated using the characteristics theory, [18].

Fig. 5 shows a three-dimensional view of the flow impinging a baffle width of 0.12 m using the ASM. Obviously, the numerical model was able to simulate the oblique waves downstream of the baffle successfully. Fig. 6 plots the numerical and experimental profiles of the flow depth in the longitudinal section p_1. The amplitude and phase of the numerical shocks are in agreement with the experimental measurements. In Fig. 7, for the sake of comparison, similar profiles 1-m downstream of the baffle along p_1, p_2 and p_3 are plotted, on a larger scale, using different turbulence models together with the case of the model without turbulence terms (WT). It may be confirmed that the results of the different models are close to each other. In other words, all of the turbulence models, and even the WT case, are able to simulate the shock behavior. However, there are some phase-lags that may be distinguished at the latter shocks amongst the different models. Apparently, the reduction of the flow velocity in the downstream channel necessitates consideration of the turbulence terms and their proper modeling. Based on these profiles, the ASM offers the most favorable results.

In Fig. 8, the contours of streamlines are plotted around a baffle of 0.24 m in width for the three turbulence models and

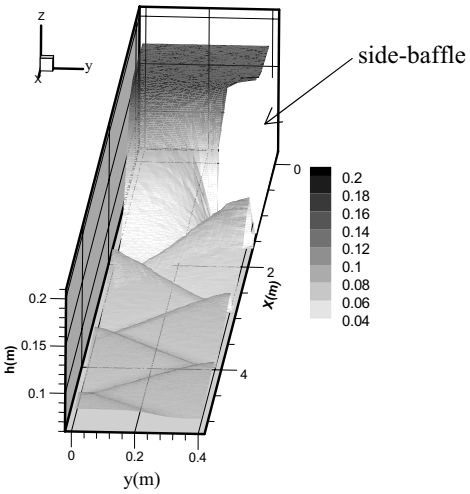

Fig. 5. 3D view of flow using ASM

Fig. 3. The experimental flume

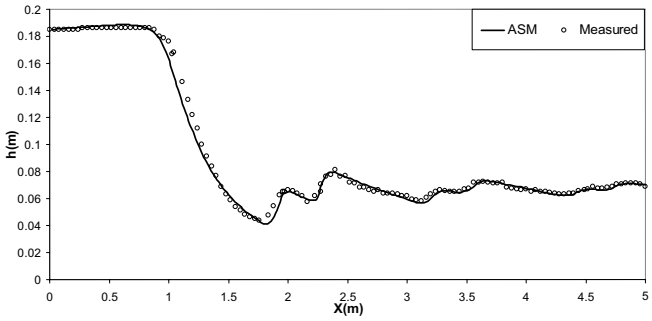

Fig. 6. Comparison between the experimental and numerical depth profiles along p_1 for a 0.12 m baffle width using ASM.

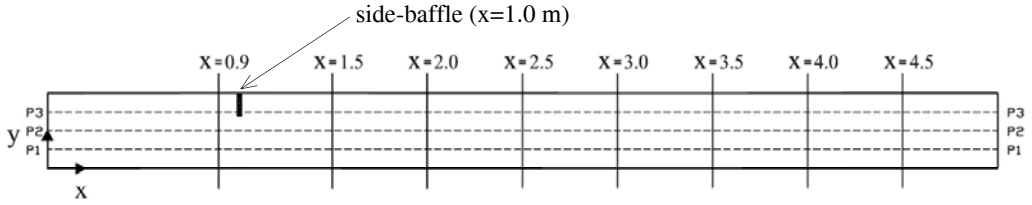

Fig. 4. The longitudinal and transversal cross sections

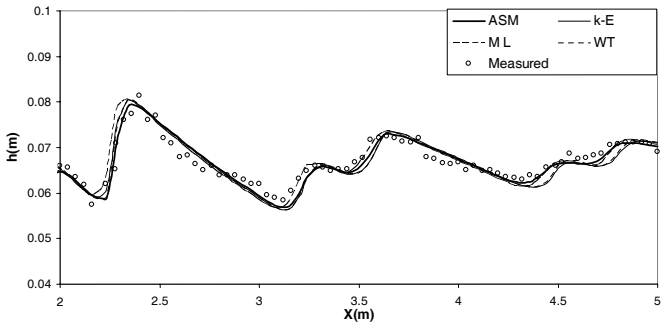

(a) along p_1

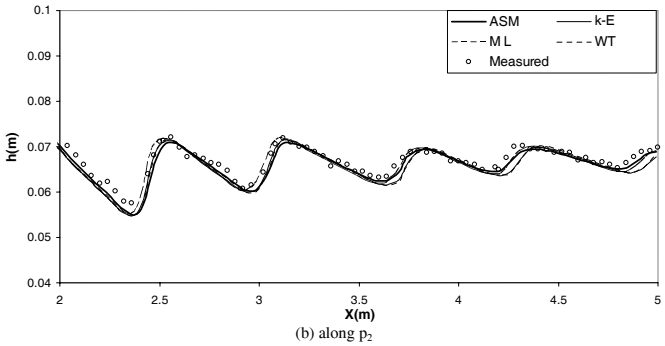

(b) along p_2

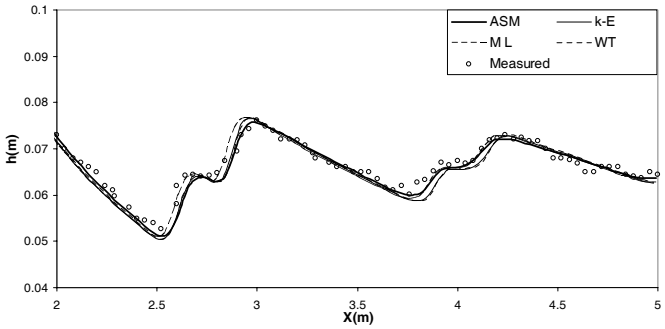

(c) along p_3

Fig. 7. Longitudinal profiles 1. m downstream from a 0.12 m baffle width

for the case lacking turbulence terms. All of the models are able to simulate a vortex adjacent to the baffle. However, the shape and length of this vortex vary in different models. In fact, the low velocity of flow at this region allows for the turbulence terms to influence the flow pattern in different models. Moreover, in the ASM and *k*-ε model, the generated vortex is stronger, and the streamlines next to the baffle are closer to each other, which is in agreement with our experimental observations. A shaded plot of the flow depth is shown in the background of this figure as well. The paths of the oblique waves are coincident with the change of the streamline directions. In Fig. 9, the distribution of the turbulence kinetic energy (*k*) for the ASM and *k*-ε model are shown in a shaded plot for a baffle width of 0.12 m. In both models, the values of *k* at the upstream side of the baffle are negligible, except in a thin margin close to the baffle due to the variation in the direction of streamlines. At the downstream canal, however, the turbulence kinetic energy is considerable, such that the position of the oblique shocks may be identified based on its variations. Based on the ASM results, the maximum value of *k* appears at the lower side of the impingement point of the first shock to the sidewall, downstream of the baffle. The *k*-ε model, however, gives larger values for *k* in a wider region at the same location.

In Figs. 10a-h, cross sectional profiles of the flow depth at various locations just before and after the baffle, obtained from different models, are compared with the measured values. It may be observed that the implementation of the turbulence models has improved the results, and the ASM shows a better performance than the other models, specifically at the standing wave fronts.

A quantitative evaluation may be obtained by comparison of the relative error norm E, defined as:

$$E = \frac{\sum |h_{num} - h_{mes}|}{\sum |h_{mes}|} \times 100 \qquad (33)$$

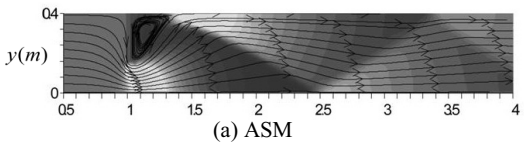

(a) ASM

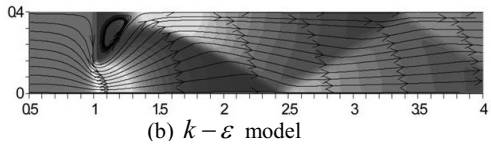

(b) $k-\varepsilon$ model

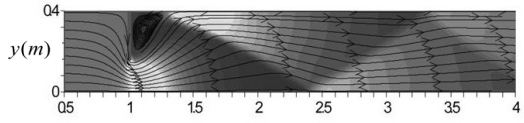

(c) Mixing length model

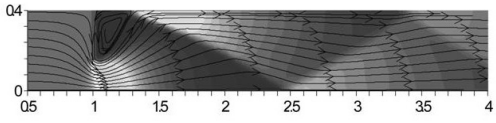

(d) Without turbulence terms

Fig. 8. Streamlines and depth shaded plots for a 0.24 m side-baffle width

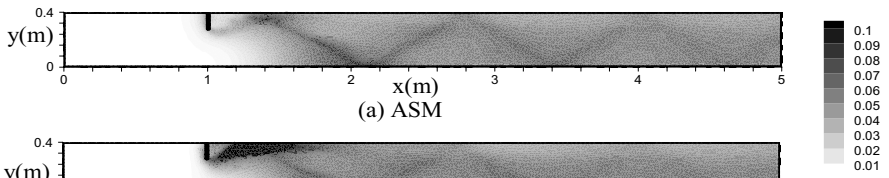

(a) ASM

(b) $k-\varepsilon$ model

Fig. 9. Shaded plots for the distribution of turbulence kinetic energy, *k* , for a 0.12 m baffle width

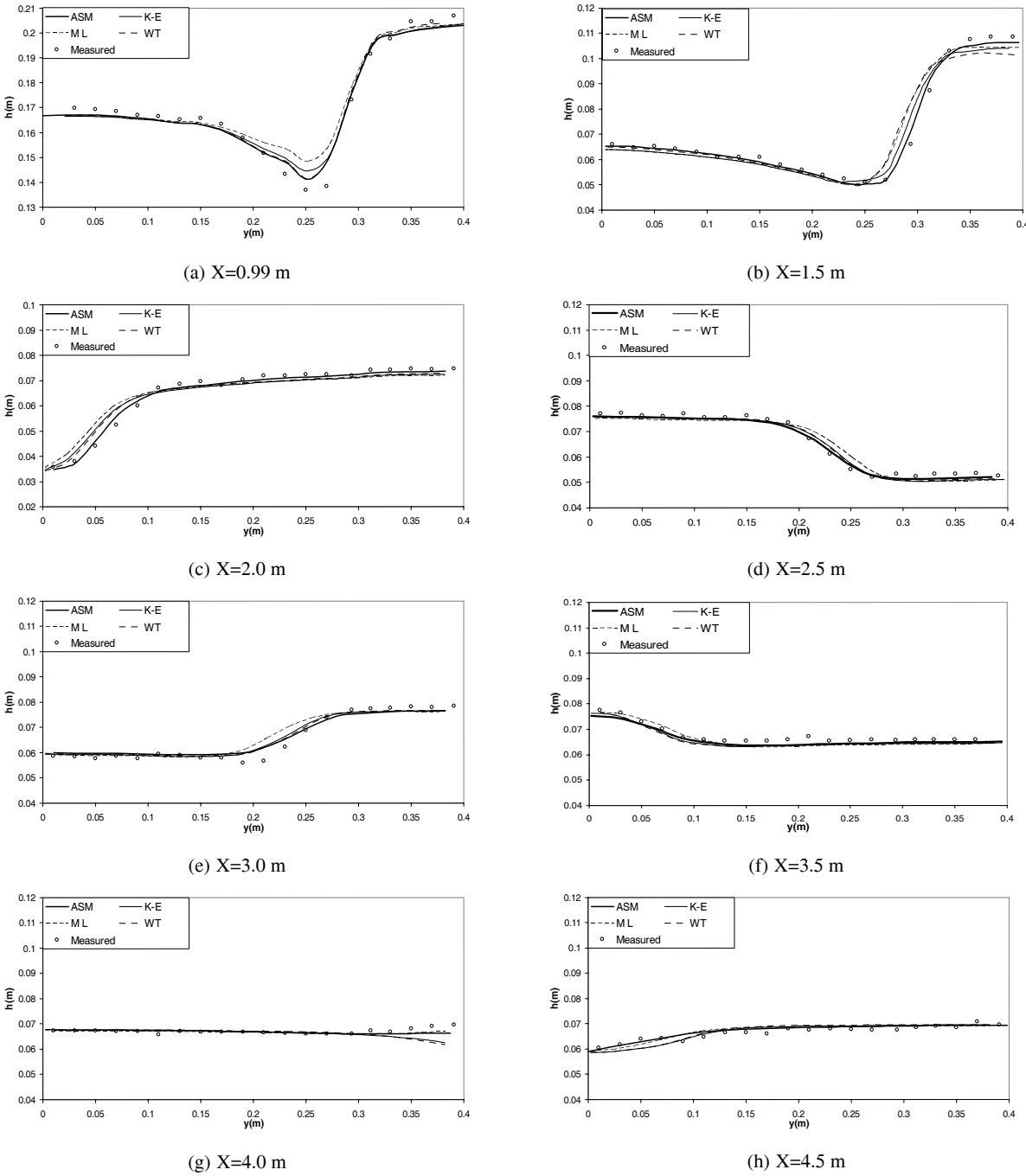

(a) X=0.99 m

(b) X=1.5 m

(c) X=2.0 m

(d) X=2.5 m

(e) X=3.0 m

(f) X=3.5 m

(g) X=4.0 m

(h) X=4.5 m

Fig. 10. Comparison between experimental and numerical transversal depth profiles for a 0.12 m side-baffle width

where h_{num} is the numerical flow depth, and h_{mes} is the measured depth. The relative error norms for the three turbulence models and the case of without turbulence terms (WT) are plotted in Fig. 11 for the longitudinal profiles p_1, p_2 and p_3 for different baffle widths. It may be concluded that the implementation of the turbulence terms reduces the error norms in all of the longitudinal cross sections and improves the results. However, in the ML model the turbulent length scale depends on water depth. This assumption is not justified crossing the oblique shock waves where a rapid variation of flow depth is observed. Moreover, the Boussinesq assumption of isotropic eddy viscosity is the main disadvantage of k-ε and ML models while in algebraic stress model Reynolds stresses are anisotropic. Consequently, the ASM presents the least error norms.

In Fig. 12, for a linear regression analysis, the computed values of depths from the ASM are drawn versus the measured depths along the p_1 and p_2 longitudinal directions. Then, a straight line was fitted to each of the data sets. The equations of the lines and R^2 coefficients for a 0.12m width baffle are shown in the graphs as well. Obviously, the numerical results are close to the experimental measurements, and the slopes of the lines approach unity. Similar graphs were plotted for other turbulence models and baffle widths. It was observed that in all of the longitudinal directions the implementation of turbulence modeling improved the numerical model, and the ASM offered the best results.

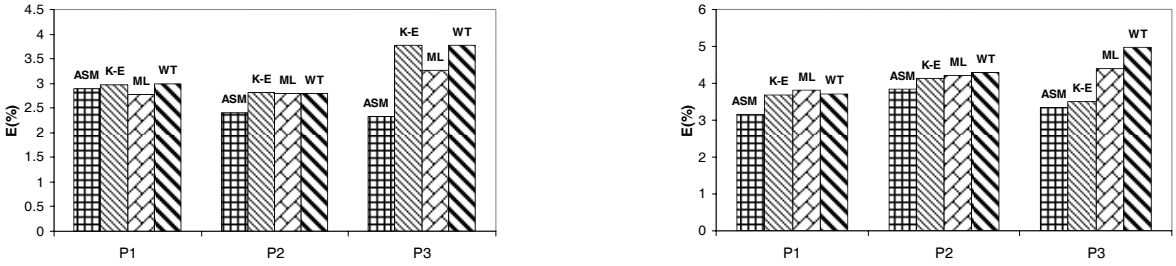

(a) Side-baffle width 0.12 m

(b) Side-baffle width 0.16 m

(c) Side-baffle width 0.24 m

(d) Side-baffle width 0.30 m

Fig. 11. Error norm E along different directions for different side-baffle widths

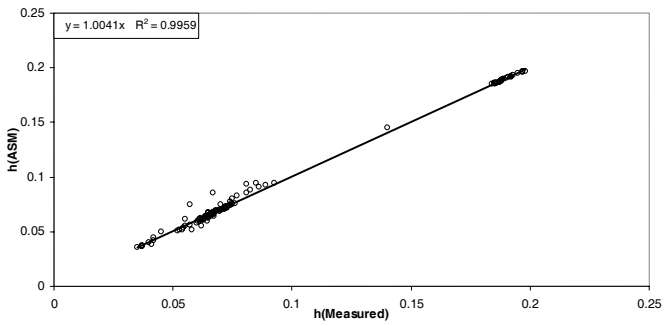

(a) along p_1

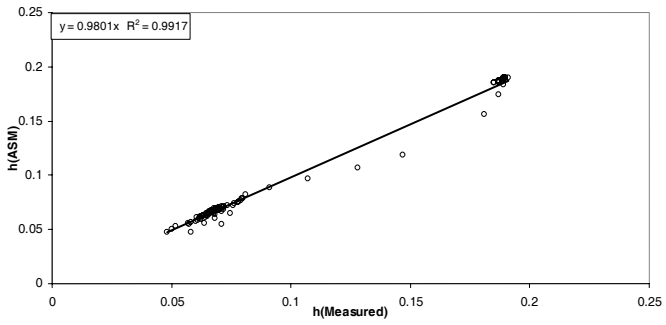

(b) along p_2

Fig. 12. Linear regression analysis

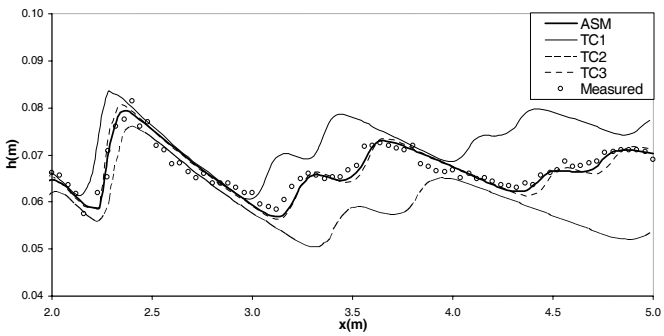

(a) along p_1

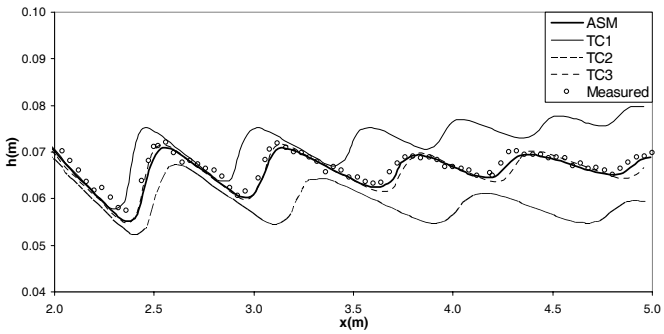

(b) along p_2

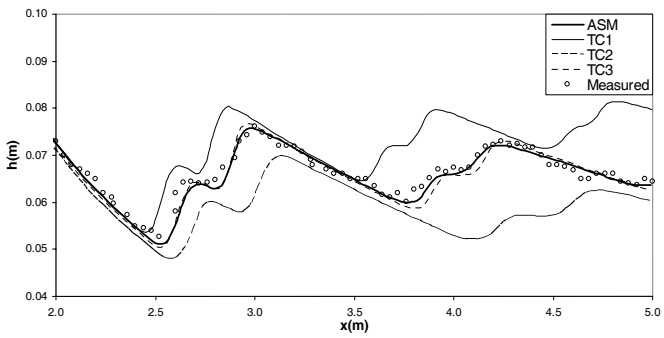

(c) along p_3

Fig. 13. Longitudinal profile of flow depth for two component of source terms, side-baffle width = 0.12 m

7. Assessment of the source term components

In Eq. (3), the source terms consist of three components; namely, the bed slope, bed friction and turbulence terms. To investigate the importance of the different components of the source terms, some numerical experiments were carried out. In each of these experiments, only one component was excluded from the source terms. Therefore, in run TC1, the bed slope term was removed; in TC2, the bed friction term was removed; and in TC3, the turbulence terms were removed. In Figs. 13 and 14,

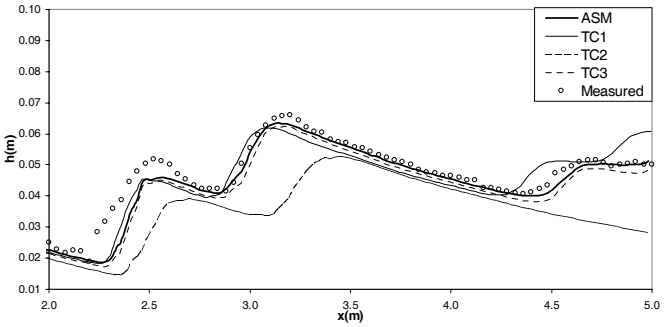

(a) along p_1

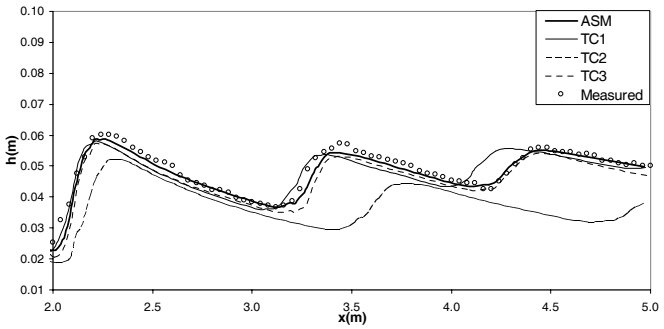

(b) along p_2

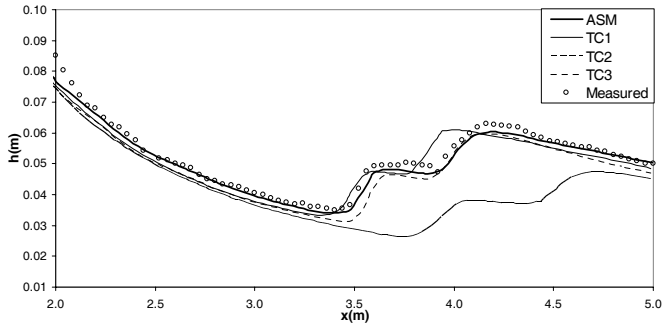

(c) along p_3

Fig. 14. Longitudinal profile of flow depth for two components of source term, side-baffle width = 0.30 m

the longitudinal profiles of the flow depths for each run along the p_1, p_2 and p_3 directions are plotted for baffle widths of 0.12 m and 0.3 m. The original profile, including all components of the source terms, (ASM), and experimental data, are also drawn in the same figures for the sake of comparison. As expected, the best results are obtained when all the components of the source terms are preserved. The shock waves in TC1 are slightly amplified with a lagging phase error and are attenuated in TC2 with a leading phase error. However, the TC3 profile, in which the bed slope and bed friction terms are retained, is close to the ASM profile and the experimental data, indicating that at least in the range of these experiments, neglecting the turbulence terms may be tolerated. This conclusion may also be reached from Fig. 11, in which the variation of the relative error norm was in a small range for all of the baffle widths. Fortunately, ignoring the turbulence terms simplifies the algorithm considerably. This finding justifies a bulk of the previous research in which the effect of the turbulence terms was completely neglected in the open channel supercritical flow computations; see, e.g., [31].

8. Conclusions

In this article, using the depth-averaged shallow water equations, the effects of several turbulence models on the performance of standing oblique shock waves were investigated. The finite volume scheme of Roe-TVD with an unstructured triangular mesh was applied. To avoid spurious oscillations at the regions where the gradients of the variable were considerable, advanced slope limiter functions were implemented in the numerical algorithm. The effects of the bed slope, bed friction and turbulences were considered in the source terms. The bed slope and bed friction terms were computed using the data at the center of each cell. Three depth-averaged turbulence models consisting of the mixing length (ML), k-ε and ASM were implemented. The standing shock depths produced by the incidence of a supercritical flow to a side-baffle were measured in a test flume. The comparison of the experimental results and numerical predictions confirmed the robustness of the numerical model. In particular, the implementation of the turbulence models improved the results at the shock positions. Moreover, all of the models were able to simulate the vortex next to the baffle successfully. However, the k-ε model and the ASM demonstrated a stronger vortex pattern. Based on our overall findings, the ASM offered superior results to the other models. The quantitative error analysis confirmed this finding as well. Our numerical experiments, however, revealed that amongst the source term components, the negligence of the turbulence terms produced the least relative depth error in comparison with the removal of the bed slope or bed friction terms.

Acknowledgement: This article is part of the PhD work of the first author. The support of the research council of Ferdowsi University of Mashhad during the preparation of this work is kindly acknowledged.

References

[1] Rodi W.: 1980, Turbulence models and their application in hydraulics, IAHR Monograph Series.

[2] Kraichnan, R.H.: 1967, Inertial ranges in two-dimensional turbulence, Journal of Physics Fluids.10,14-17.

[3] Batchelor, G.K.: 1969, Computation of the energy spectrum in homogeneous two-dimensional turbulence, Journal of Physics Fluids Suppl.II. 233-239.

[4] Dracos, T., Gigerm, M. and Jirka, G.H.:1992, Plane turbulent jets in a bounded fluid layer, Journal of Fluid Mechanics.241, 587-614.

[5] Giger, M. Dracos, T. and Jirka, G.H.: 1979, Entrainment and mixing in plane turbulent jets in shallow water, Journal of Hydraulic Research.29, 615-643.

[6] Chen, D. and Jirka, G.H.: 1998, Linear instability analysis of turbulent mixing layers and jets in shallow water layers, Journal of Hydraulic Research.36, 525-253.

[7] Thomas, F.O.:1986, Goldschmidt VW. Structural characteristics of developing turbulent planar jet, Journal of Fluid Mechanics.63, 227-256.

[8] Lloyd, P.M., Stansby, P.K. and Chen, D.: 2001, Wake formation around islands in oscillatory laminar shallow water Flows, Journal of Fluid Mechanics.429, 217-238.

[9] Uijttewaal, W.S.J., and Girka, G.H.: 2003, Grid turbulence in shallow flows, Journal of Fluid Mechanics.489, 325-344.

[10] Uijttewaal, W.S.J. and Booij, R.:2000, Effects of shallowness on the development of free-surface mixing layers, Journal of Physics Fluids.12, 392-402.
[11] Uijttewaal, W.S.J. and Tukker, J.: 1998, Development of quasi two-dimensional structures in a shallow free-surface mixing layer, Journal of Experimental Fluids.24, 192-200.
[12] Chu, V.H. and Babarutsi, S.: 1998, Confinement and bed-friction effects in shallow turbulent mixing layers, Journal of Hydraulic Engineering.114, 1257-1274.
[13] Vazquez-Cendon, M.E., Cea, L. and Puertas, J.: 2009, The shallow water model: The relevance of geometry and turbulence, Monografias de la Real Academia de Ciencias de Zaragoza.31, 217–236.
[14] Cea, L. and Vazquez-Cendon, M.E.: 2008, Depth averaged turbulence models and source terms, Numerical Modelling of Hydrodynamics for Water Resources, Taylor & Francis Group.
[15] Jia, Y. and Wang, S.S.Y.: 1999, Numerical model for channel flow and morphological change studies, Journal of Hydraulic Engineering.125, 924–933.
[16] Rastogi, A.K. and Rodi, W.: 1978, Predictions of heat and mass transfer in open channels, Journal of the Hydraulics Division. 397-420.
[17] Cea, L., Jeronimo, P. and Vazquez-Cendon, M.E.: 2007, Depth averaged modeling of turbulent shallow water flow with wet-dry fronts, Archives of Computational Methods in Engineering.14, 303–341.
[18] Toro, E.F.: 2001, Shock-capturing methods for free-surface shallow flows, Wiley, Chichester.
[19] Leveque, R.J.: 2002, Finite volume methods for hyperbolic problems, Cambridge University Press.
[20] Roe, P.L.: 1981, Approximate Riemann solvers, parameter vectors, and difference schemes, Journal of Comput Physics.43, 357–372.
[21] Osher, S. and Solomon, F.: 1982, Upwind difference schemes for hyperbolic systems of conservation laws, Math. Comp.38, 339–374.
[22] Harten, A., Lax, P.D. and van Leer, B.: 1983, On upstream differencing and Godunov-type schemes for hyperbolic conservation laws, SIAM Rev. 25, 35–61.
[23] Einfeldt, B.: 1988, On Godunov-type methods for gas dynamics, SIAM J. Numer. Anal. 25, 294–318.
[24] Trangenstein, J.A.: 2007, Numerical solution of hyperbolic partial differential equations, Cambridge University Press.
[25] Cea, L.:2005, An unstructured finite volume model for unsteady turbulent shallow water flow with wet-dry fronts, numerical solver and experimental validation, Doctoral Thesis, Departamento de Metodos Matematicos y de Representacion, Universidad de A Coruna.
[26] Yoon, T.H, and Kang, S.: 2004, Finite volume model for two-dimensional shallow water flows on unstructured grids, Journal of Hydraulic Engineering. 130, 678-688.
[27] Davidson, L.: 1993, Implementation of a model and a Reynolds Stress Model into a multiblock code, Tech. Rep. CRS4-APPMATH-93-21, Applied Mathematics and Simulation Group CRS4, Cagliary, Italy.
[28] Hajivalie, F, and Yeganeh Bakhtiary, A.: 2011, Numerical simulation of the interaction of a broken wave and a vertical breakwater, International Journal of Civil Engineering. 9, 71-79.
[29] Durbin, P.: 1996, On the stagnation point anomaly, Int. J. Heat Fluid Flow.17, 89-90.
[30] Davidson, L.: 1997, An introduction to turbulence models, Tech Rep 97/2, Dept of Thermo and Fluid Dynamics, Chalmers University of Technology.
[31] Chaudhry, M.H.: 2008, Open-Channel Flow, Second Edition. Springer.